Review

An Update Review on *N*-Type Layered Oxyselenide Thermoelectric Materials

Junqing Zheng, Dongyang Wang * and Li-Dong Zhao *

School of Materials Science and Engineering, Beihang University, Beijing 100191, China; sy1901125@buaa.edu.cn
* Correspondence: wangdongyang@buaa.edu.cn (D.W.); zhaolidong@buaa.edu.cn (L.-D.Z.)

Abstract: Compared with traditional thermoelectric materials, layered oxyselenide thermoelectric materials consist of nontoxic and lower-cost elements and have better chemical and thermal stability. Recently, several studies on *n*-type layered oxyselenide thermoelectric materials, including BiCuSeO, Bi_2O_2Se and $Bi_6Cu_2Se_4O_6$, were reported, which stimulates us to comprehensively summarize these researches. In this short review, we begin with various attempts to realize an *n*-type BiCuSeO system. Then, we summarize several methods to optimize the thermoelectric performance of Bi_2O_2Se, including carrier engineering, band engineering, microstructure design, et al. Next, we introduce a new type of layered oxyselenide $Bi_6Cu_2Se_4O_6$, and *n*-type transport properties can be obtained through halogen doping. At last, we propose some possible research directions for *n*-type layered oxyselenide thermoelectric materials.

Keywords: thermoelectric; *n*-type oxyselenide; BiCuSeO; Bi_2O_2Se; $Bi_6Cu_2Se_4O_6$

1. Introduction

Thermoelectric (TE) materials can achieve the direct transition between heat and electricity without producing other pollutants, providing an effective solution to the energy crisis and environmental problems [1,2]. The dimensionless figure of merit *ZT* defines the efficiency of a thermoelectric device, which derives from three related physical quantities: electrical conductivity (σ), Seebeck coefficient (*S*) and thermal conductivity (κ), $ZT = (\sigma S^2 T / \kappa)$, with absolute temperature *T*. However, the tightly-coupled relationship among these parameters makes it difficult to improve the overall *ZT* [2–6].

Compared with traditional thermoelectric materials, such as Bi_2Te_3 [7–10], PbTe [11–15], SnTe [13,16], MgAgSb [17–19], half-Heusler alloys [20–22], Zintl phases [23,24], etc., layered oxyselenide thermoelectric materials, mainly including BiCuSeO [2,25], Bi_2O_2Se [26,27] and $Bi_6Cu_2Se_4O_6$ [28–30], consist of earth-abundant, nontoxic, light and lower-cost elements, and have better chemical and thermal stability in the middle temperature range (600–900 K) [2,31]. Therefore, this series was regarded as thermoelectric materials with broad development prospects and studied extensively.

Intrinsic *p*-type semiconductor BiCuSeO possesses a layered ZrCuSiAs structure with space group *P4/nmm* [2,32]. The special layered crystal structure of BiCuSeO is constituted by insulative $[Bi_2O_2]^{2+}$ layers and conductive $[Cu_2Se_2]^{2-}$ layers heaping along the *c*-axis by turns [33,34]. Due to the weak Van der Waals interaction between layers [9,35–37], the large displacement of the Cu atom [38,39] and the heavy Bi atom [3,40,41], BiCuSeO has intrinsically low thermal conductivity [42], which is an inherent advantage as a thermoelectric material. However, most of the reported BiCuSeO are *p*-type semiconductor materials at present, and researches on *n*-type BiCuSeO are relatively few and unsuccessful. The main problems are that no effective electronic dopant was found, and BiCuSeO-based materials with stable *n*-type transport properties have not been obtained yet.

Different from BiCuSeO, the intrinsic Bi_2O_2Se exhibits *n*-type transport properties due to a large number of Se vacancies in the crystal structure [43,44]. However, the crystal

structure of Bi_2O_2Se is very similar to BiCuSeO in which insulative $[Bi_2O_2]^{2+}$ layers and conductive $[Se]^{2-}$ layers stack along the *c*-axis alternatively [26,45,46]. Similarly, Bi_2O_2Se also has intrinsically low thermal conductivity due to the weak interlayer interaction [26,47–49], but its intrinsic carrier concentration ($\sim 1.5 \times 10^{15}$ cm^{-3}) is too low, resulting in poor electrical transport performance [50,51]. Therefore, current research is mainly focused on increasing the carrier concentration, thus improving the electrical transport performance of Bi_2O_2Se.

$Bi_6Cu_2Se_4O_6$ is a new type of layered oxyselenide thermoelectric material [28–30]. The crystal structure of $Bi_6Cu_2Se_4O_6$ can be regarded as a 1:2 ratio of BiCuSeO and Bi_2O_2Se heaping along the *c*-axis by turns [28], so there are insulative layers $[Bi_2O_2]^{2+}$ and conductive layers $[Cu_2Se_2]^{2-}$ and $[Se]^{2-}$ in the structure. The $Bi_6Cu_2Se_4O_6$ system not only maintains the low thermal conductivity of BiCuSeO but also can utilize the intrinsic electron carrier concentration of Bi_2O_2Se, considered to be a promising *n*-type oxyselenide thermoelectric material. At present, the $Bi_6Cu_2Se_4O_6$ system with stable *n*-type transport properties can be obtained by halogen doping [29], and strategies to improve its thermoelectric performance need to be further explored.

Recently, several studies on *n*-type layered oxyselenide thermoelectric materials were reported, which motivates us to systematically summarize the recent progress of these researches. The outline of this review is shown in Figure 1. First, several attempts to realize *n*-type BiCuSeO are summarized. Then, some typical approaches to optimize the thermoelectric performance of Bi_2O_2Se are presented. Next, a new type layered oxyselenide $Bi_6Cu_2Se_4O_6$ is introduced, and *n*-type transport properties can be obtained through halogen doping and optimized by introducing transition metal elements. At last, some prospective and outlooks were provided for future research in the end.
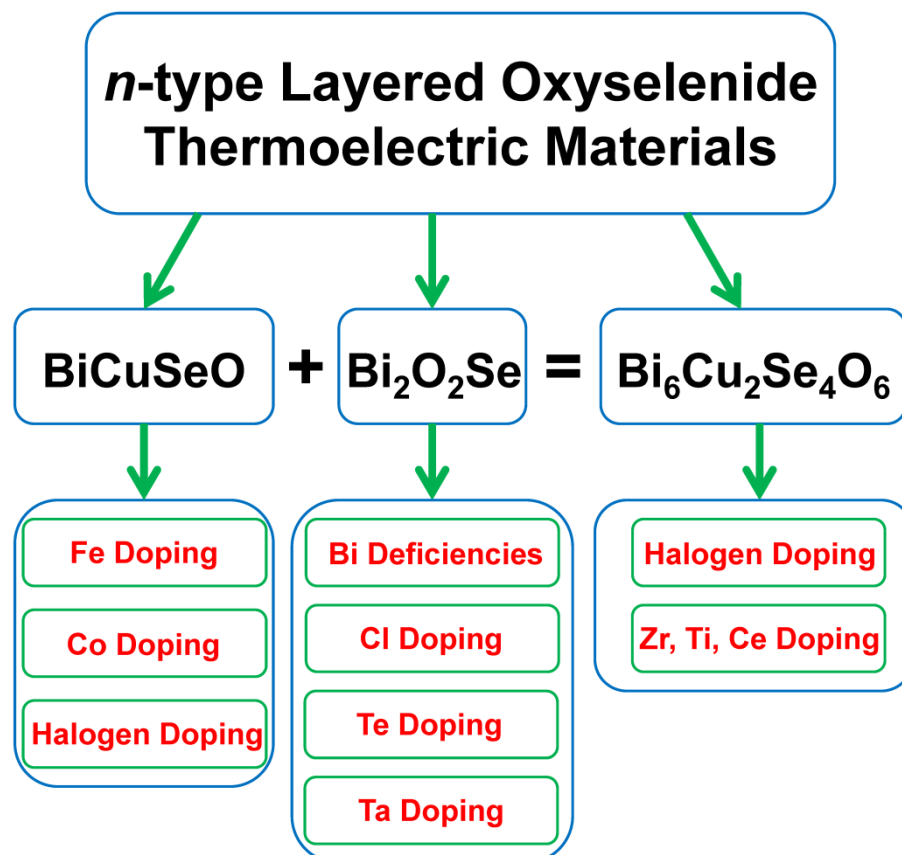

Figure 1. The outline of this review.

2. Various Attempts to Realize *n*-Type BiCuSeO

2.1. Doping Fe at Cu Sites

Pan et al. obtained *n*-type transport properties in the BiCuSeO system in the low-temperature range (300–500 K) through doping Fe at Cu sites [52]. Figure 2a,b display the temperature-dependent electrical conductivity (σ) and Seebeck coefficient (S) for Fe-doped samples. The σ of all samples increases monotonically with temperature, showing semiconductor conduction behavior. Meanwhile, at the same temperature, the σ increases with the increasing Fe content, indicating that Fe is an effective dopant for pristine BiCuSeO matrix. The peak values of S for samples $BiCu_{1-x}Fe_xSeO$ ($x = 0$ to 0.03) are larger than 150 $\mu V\ K^{-1}$ and shift towards higher temperature with the increasing Fe content. The band gap can be estimated by the peak value of S through the Goldsmid–Sharp law as Formula (1) [53,54]:

$$E_g = 2e|S|_{max}T \tag{1}$$
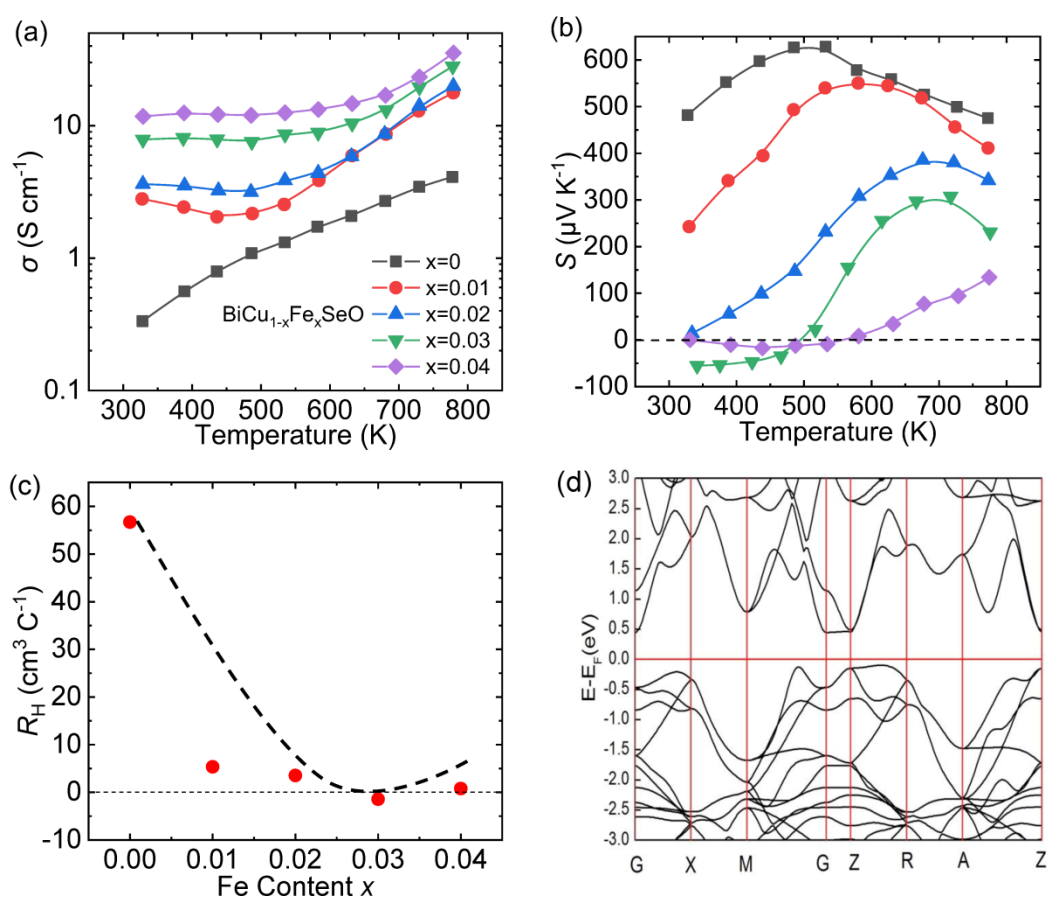
Figure 2. The curves of (**a**) electrical conductivity, and (**b**) Seebeck coefficient varying with temperature for $BiCu_{1-x}Fe_xSeO$ ($x = 0$ to 0.04); (**c**) Fe content dependences of Hall coefficient for $BiCu_{1-x}Fe_xSeO$ ($x = 0$ to 0.04) at room temperature. Data presented in (**a**–**c**) were adopted from Reference [52]. Copyright 2018, The Royal Society of Chemistry. (**d**) Calculated band structure of pristine BiCuSeO near the Fermi level. Copyright, the Royal Society of Chemistry. (**d**) Reproduced with permission from Reference [55]. Copyright 2019, Elsevier Masson SAS.

The peak Seebeck coefficient and corresponding temperature increase with the increase in Fe content, indicating the increase of band gap in those samples. Clearly, *n*-type transport properties can be found in the $x = 0.03$ sample at a low-temperature range, indicating that appropriate Fe content can achieve *n*-type BiCuSeO in a circumscribed temperature range.

The variation of Hall coefficient (R_H) at room temperature is presented in Figure 2c. Expectedly, BiCuSeO-based materials exhibit *p*-type electrical transport properties, and

R_H should be positive. However, the R_H of $BiCu_{0.97}Fe_{0.03}SeO$ exhibits a negative value, confirming the *n*-type behavior conjectured by the negative *S*. The transition of electrical transport properties can be explained by the following two formulas [56,57]:

$$R_H = \frac{n_h\mu_h^2 - n_e\mu_e^2}{e(n_h\mu_h + n_e\mu_e)^2} \tag{2}$$

$$S = \frac{S_h\sigma_h + S_e\sigma_e}{\sigma_h + \sigma_e} \tag{3}$$

where, subscripts *h* and *e* express hole and electron carriers, respectively. In the above two formulas, n_h and n_e are both positive, while S_h and S_e are positive and negative, respectively. The decline of R_H and *S* after doping Fe in Cu sites can be explained by the competition between the intrinsic holes and the electrons introduced by Fe substitution, which indicates that the substitution of Fe for Cu is a kind of donor doping. When the Fe content increases to 0.03, σ increases due to the increasing total carrier concentration ($n_t = n_h + n_e$); while *S* declines because the negative contribution of electrons partly counterbalances the positive contribution of holes to *S*, ultimately switching to negative when electrons become majority carriers. Figure 2d exhibits the calculated band structure of pristine BiCuSeO. The valence band maximum (VBM) and conduction band minimum (CBM) are located along the Γ-M and Γ-Z direction, respectively. Larger degeneracy of VBM than CBM leads to a less favorable compromise between large mobility and large effective mass, so the large *S* values are not easy to obtain *n*-type transport.

2.2. Doping Co at Cu Sites

Ren et al. aimed to increase the Seebeck coefficient by introducing magnetic ions into the BiCuSeO matrix because previous studies on other systems showed that extra spin entropy could be introduced by the magnetic ions, thereby contributing to increasing the Seebeck coefficient [55]. They found that the BiCuSeO system exhibits *n*-type electrical transport properties below room temperature when the Co content reaches 20%.
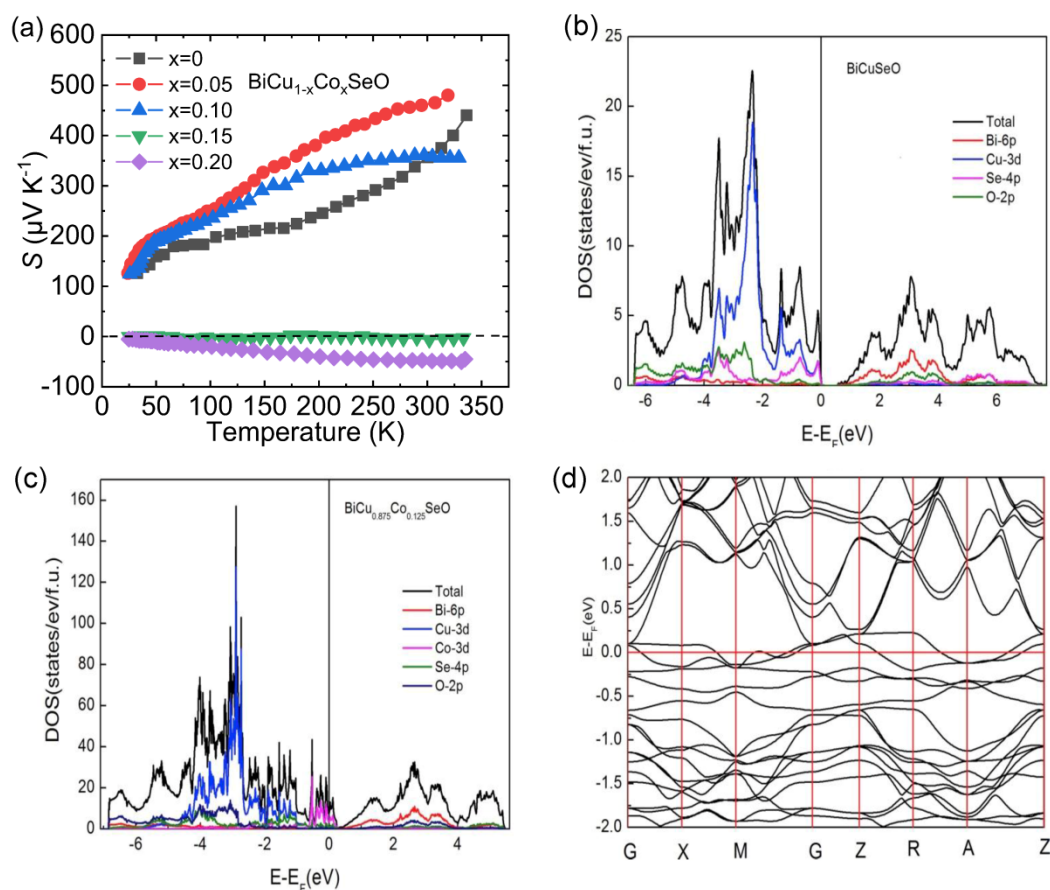
Figure 3a shows the temperature-dependent Seebeck coefficient (*S*) for Co-doped samples. For *x* = 0.05 and 0.10 samples, the *S* is positive within the entire temperature boundaries, indicating the dominant carrier is *p*-type. However, when the doping content of Co reaches 15%, the *S* begins to appear negative, indicating that the system exhibits *n*-type electrical transport properties. The negative *S* values of *x* = 0.20 sample within the entire temperature region indicate stable *n*-type electrical transport properties in the BiCuSeO system below room temperature.

The VBM of BiCuSeO mainly comes from the hybridization between Cu 3*d* and Se 4*p* orbitals, while the CBM is derived from the Bi 6*p* orbital [2,58,59], as shown in Figure 3b. For $BiCu_{0.875}Co_{0.125}SeO$, the DOS close to Fermi level mainly derives from the Co 3*d* and Se 4*p* orbitals (Figure 3c), and the number of bands crossing the Fermi level is two (Figure 3d), which are both electron cylinder and hole cylinder, indicating the Co substitution introduces *n*-type carriers [60]. It can be seen that Co substitution can change the band structure of BiCuSeO and make the Fermi level reach to the CBM. When the Co content is large enough, electrons become majority carriers.

2.3. Doping Halogen (Br, I) at Se Sites

Zhang et al. designed a series of continuous experimental steps to obtain *n*-type BiCuSeO [61]. Firstly, considering that the existence of Bi/Cu vacancies is the main reason for the *p*-type behavior of pristine BiCuSeO [62,63], extra Bi/Cu was introduced into the matrix to fill the vacancies which may produce holes. Finally, the optimal concentrations of extra Bi and Cu are determined as *x* = 0.04 and 0.05, respectively. To increase electron carrier concentration, halogen elements (Br, I) were selected as donor dopants at Se sites and introduced into the $Bi_{1.04}Cu_{1.05}SeO$ matrix. The *S* as a function of temperature for I/Br doped $Bi_{1.04}Cu_{1.05}SeO$ samples is presented in Figure 4a,b. The introduction of Br/I can

successfully transform $Bi_{1.04}Cu_{1.05}SeO$ from *p*-type to *n*-type within a certain temperature range, and the negative *S* for I-doped $Bi_{1.04}Cu_{1.05}SeO$ traverses a narrower temperature range than Br-doped one. In the high-temperature range, *p*-type behavior appears again, indicating that vacancies reproduced as the temperature rises, which may be relevant to the instability of Cu–Br and Cu–I bonds [64,65].
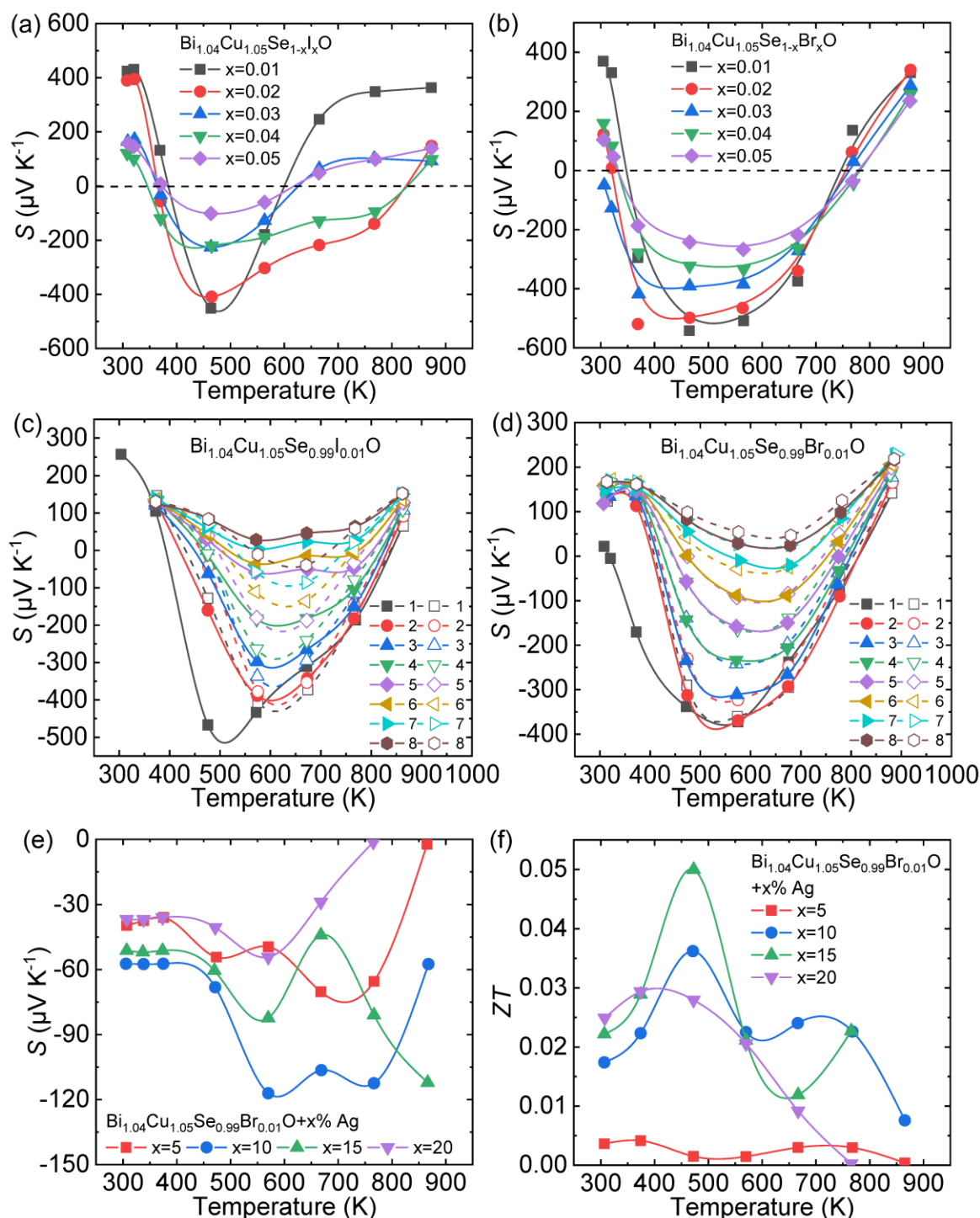

Figure 3. (**a**) The temperature-dependent Seebeck coefficient of $BiCu_{1-x}Co_xSeO$ (*x* = 0.05–0.20). Data were adopted from Reference [55]. Copyright 2019, Elsevier Masson SAS. Calculated density of states (DOS) of (**b**) BiCuSeO and (**c**) $BiCu_{0.875}Co_{0.125}SeO$, and (**d**) electronic band structure of $BiCu_{0.875}Co_{0.125}SeO$. (**b**–**d**) Reproduced with permission from Reference [55]. Copyright 2019, Elsevier Masson SAS.

In order to further explore the *p-n-p*-type behavior in the obtained system, a heating–cooling measurement was carried out for halogen doing BiCuSeO samples [66], as shown in Figure 4c,d. As can be seen, $Bi_{1.04}Cu_{1.05}Se_{0.99}X_{0.01}O$ (*X* = Br, I) changes completely from *n*-type to *p*-type transport behavior after eight heating–cooling cycle measurements. The above results indicate that halogens are effective dopants to obtain *n*-type BiCuSeO but exhibit poor stability. To improve the stability of *n*-type transport, metallic particles were introduced into the halogen-doped $Bi_{1.04}Cu_{1.05}SeO$. The temperature dependence of *S* for $Bi_{1.04}Cu_{1.05}Se_{0.99}Br_{0.01}O$ + *x*% Ag samples is negative within the entire temperature range, and the maximum |*S*| is ~125 μV/K (Figure 4e). The maximum *ZT* ~0.05 can be reached at 475 K in $Bi_{1.04}Cu_{1.05}Se_{0.99}Br_{0.01}O$ + 15% Ag (Figure 4f).

To further understand the instability of halogen doping in BiCuSeO, the energy integrated Crystal Orbital Hamiltonian Population (ICOHP) values were calculated (Figure 5) [66]. The more negative value of ICOHP indicates the stronger bond strength [67]. As can be seen in Figure 5, after halogen doping, the ICOHP value decreases from ~1.09 eV for Cu–Se to ~0.36 eV for Cu–I, ~0.25 eV for Cu–Br and ~0.13 eV for Cu–Cl, respectively, indicating

the weaker bond strength due to halogen doping. The weakened bond strength led to the instability of halogen doping in the BiCuSeO system under the heating–cooling cycle.

Figure 4. The temperature dependence of Seebeck coefficient for (**a**) $Bi_{1.04}Cu_{1.05}Se_{1+x}I_xO$ (x = 0.01–0.05) and (**b**) $Bi_{1.04}Cu_{1.05}Se_{1+x}Br_xO$ (x = 0.01–0.05). The temperature-dependent Seebeck coefficients obtained through heating-cooling cycle measurements: 8 cycles for (**c**) $Bi_{1.04}Cu_{1.05}Se_{0.99}I_{0.01}O$ and (**d**) $Bi_{1.04}Cu_{1.05}Se_{0.99}Br_{0.01}O$, respectively. The solid symbols and lines express the heating process, while the dashed symbols and lines express cooling process. The temperature dependence of (**e**) Seebeck coefficients and (**f**) ZT value of $Bi_{1.04}Cu_{1.05}Se_{1+x}Br_xO + x\%$ Ag (x = 5–20). Data shown in (**a**,**b**,**e**,**f**) were adopted from Reference [61]. Copyright 2017, Elsevier Inc. Data shown in (**c**–**d**) were adopted from Reference [66]. Copyright 2019, Elsevier Ltd and Techna Group S.r.l.
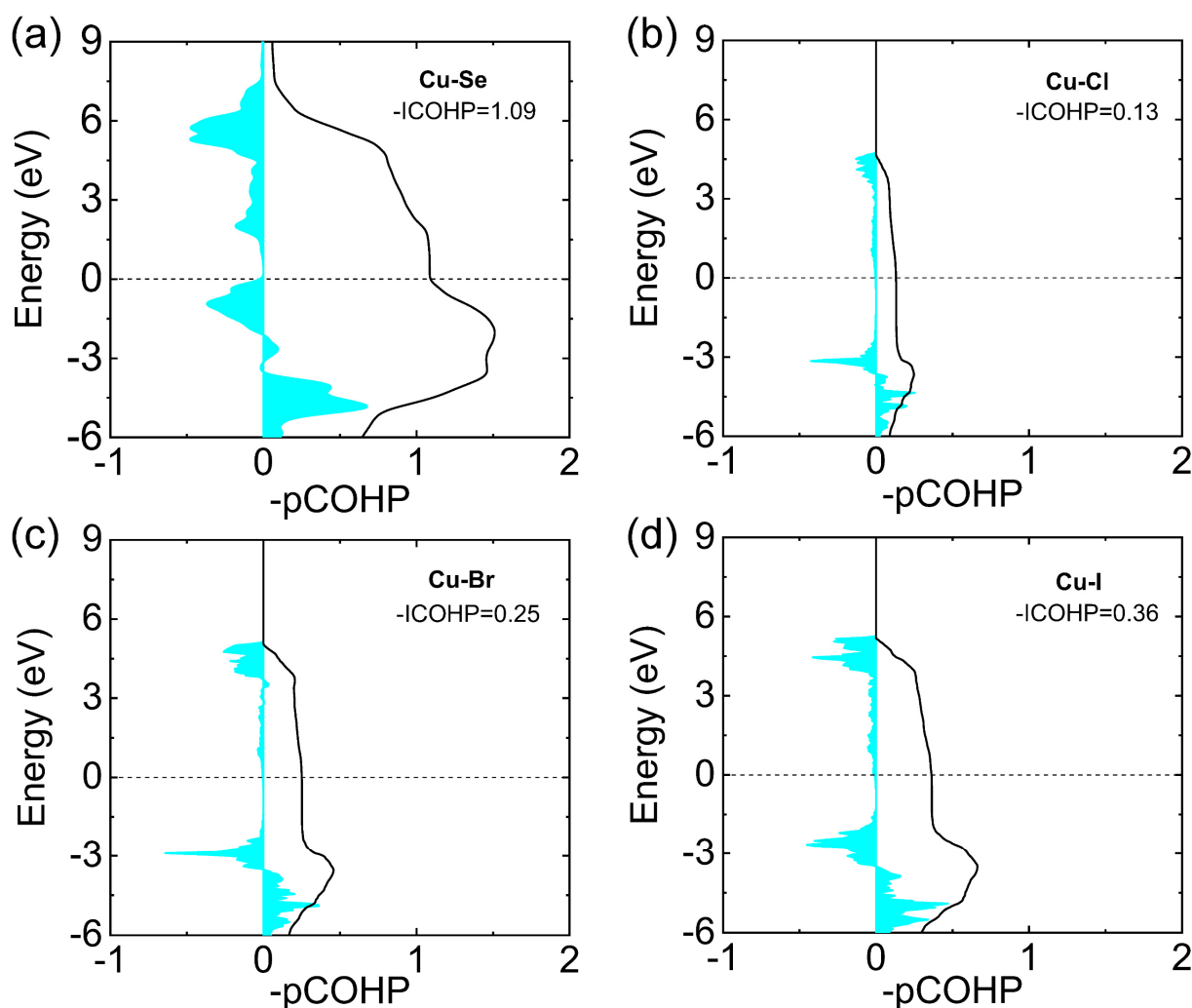
Figure 5. The energy integrated Crystal Orbital Hamiltonian Population (ICOHP) values for (**a**) Cu–Se bonding in BiCuSeO, (**b**) Cu–Cl bonding in $Bi_{1.04}Cu_{1.05}Se_{0.99}Cl_{0.01}O$, (**c**) Cu–Br bonding in $Bi_{1.04}Cu_{1.05}Se_{0.99}Br_{0.01}O$ and (**d**) Cu–I bonding in $Bi_{1.04}Cu_{1.05}Se_{0.99}I_{0.01}O$. Data in (**a**–**d**) were adopted from Reference [66]. Copyright 2019, Elsevier Ltd and Techna Group S.r.l.

## 3. Various Attempts to Enhance Thermoelectric Properties of Bi_2O_2Se

3.1. Introduce Bi Deficiencies

Due to a large number of Se vacancies in the crystal structure, the pristine Bi_2O_2Se exhibits *n*-type semiconductor behavior [43,44]. To improve the conductivity of Bi_2O_2Se, thereby optimizing its *ZT*, the general approach is to do donor doping at the Bi/Se sites [47,51,68]. However, Zhan et al. made an innovative attempt that introduces Bi deficiencies into Bi_2O_2Se by components deviating from the stoichiometric ratio [46]. In fact, the introduction of Bi deficiencies is equivalent to acceptor doping to the matrix, which runs counter to the general method. However, the increment of Seebeck coefficient and the decrease in thermal conductivity caused by the introduction of Bi deficiencies have optimized the thermoelectric properties of Bi_2O_2Se.

The introduction of Bi deficiencies has little effect on the electric conductivity (σ) of the Bi_2O_2Se system, but it can significantly change the Seebeck coefficient (*S*). The absolute values of *S* increased first and then decreased with temperature but always kept a large peak value (-445.6, -556.6, -490.0 and -568.8 $\mu V/K$ at 773 K, respectively), as shown in Figure 6a. When the carrier concentration in the semiconductor is very low, the *S* can be

evinced as the following Formula (4) [4]:

$$S = \frac{8\pi^2 k_B^2}{3eh^2} m^* T \left(\frac{\pi}{3n}\right)^{2/3} \tag{4}$$

where k_B, e, h, m^*, T and n mean Boltzmann constant, electron charge, Plank constant, the effective mass of carrier, the absolute temperature and the carrier concentration, respectively.
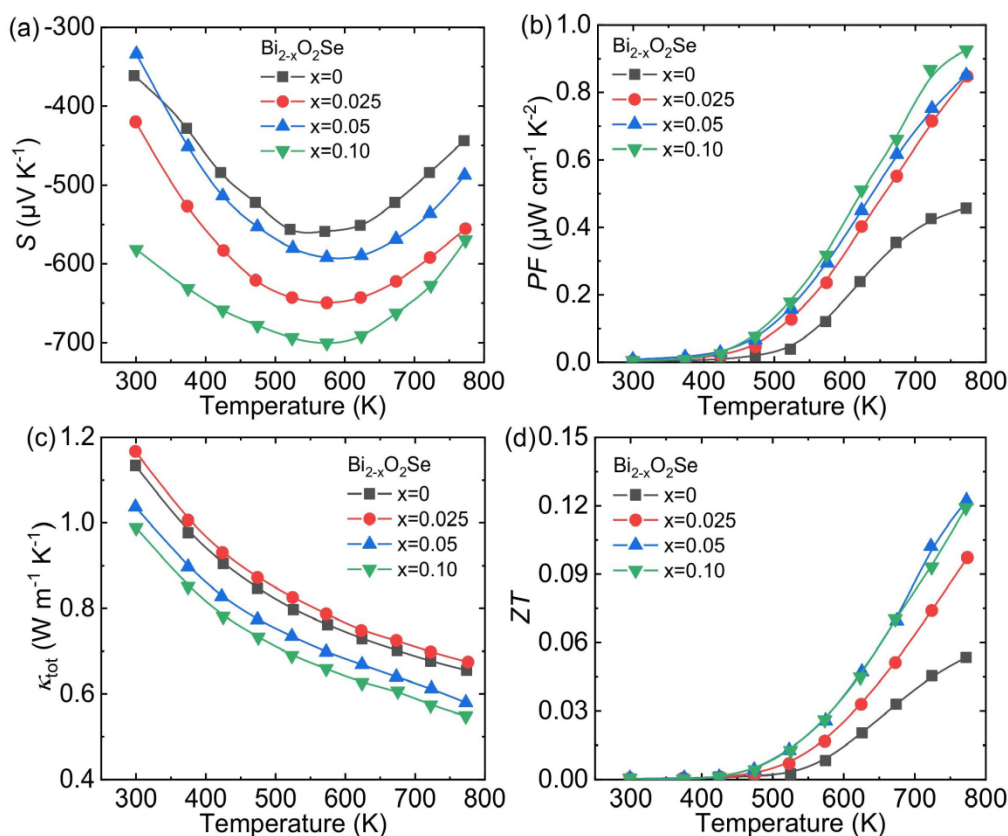
Figure 6. The temperature-dependent thermoelectric transport properties of $Bi_{2-x}O_2Se$ (x = 0–0.10): (**a**) Seebeck coefficient, (**b**) power factor, (**c**) total thermal conductivity and (**d**) ZT. Data shown in (**a**–**d**) were adopted from Reference [46]. Copyright 2015, The American Ceramic Society.

The S at low temperature increases proportionally with temperature for a given carrier concentration and effective mass. The intrinsic excitation at high temperature is enhanced, and the effective carrier concentration increases, so the S decreases. Furthermore, the S of Bi deficiencies samples are basically larger than pristine Bi_2O_2Se within the entire temperature range, which can be attributed to the influence of m^*. Thanks to the significant improvement of S, the PF peak value reaches ~0.93 $\mu W\ cm^{-1}\ K^{-2}$ at 773 K (Figure 6b), which is twice that of the intrinsic sample (~0.45 $\mu W\ cm^{-1}\ K^{-2}$ at 773 K). The Bi deficiencies strengthen the point defect scattering and lead to a decrease of κ_{tot} (Figure 6c). Integrating the enhanced electrical properties and suppressed thermal properties, the peak ZT value reaches ~0.12 in $Bi_{1.9}O_2Se$ at 773 K (Figure 6d).

3.2. Doping Cl at Se Sites

In the special crystal structure of Bi_2O_2Se, the $[Se]^{2-}$ layer is considered to be an electron-conducting pathway [43,44,46]. Therefore, effective electron donor dopants can be used to modify the conductive $[Se]^{2-}$ layer to increase the carrier concentration of the Bi_2O_2Se system, thereby enhancing its thermoelectric performance. Tan et al. doped Cl at Se sites and achieved an extraordinary enhancement in the electrical conductivity of the Bi_2O_2Se system [51].

At room temperature, the σ hikes from ~0.019 S cm^{-1} for Bi$_2$O$_2$Se to ~101.6 S cm^{-1} for Bi$_2$O$_2$Se$_{0.985}$Cl$_{0.015}$, and then declines obviously as the Cl content increases (Figure 7a). One Cl$^-$ doped into the Se^{2-} sites can provide an extra electron, and the measured carrier concentration increased from 1.5×10^{15} cm^{-3} to 1.38×10^{20} cm^{-3} ($x = 0.015$). However, when the Cl content exceeds the solubility limit, the formation of the low-conductivity second phase Bi$_{12}$O$_{15}$Cl$_6$ [69] will reduce the effective doping amount of Cl, thereby deteriorating the σ. The small polaron hopping conduction theory was chosen to study the impact of Cl dopant on the σ. This theory could be expressed as the following Formula (5) [70]:

$$\sigma = ne\mu = \left(\frac{C}{T}\right) \exp\left(\frac{-E_a}{k_B T}\right) \tag{5}$$

where n, e, μ, C, k_B, E_a and T express the carrier concentration, carrier charge, carrier mobility, the pre-exponential terms, Boltzmann constant, activation energy and the absolute temperature, respectively. Figure 7b shows the linear relationship between $\ln(\sigma T)$ and $1000/T$, and the E_a can be obtained by calculating the slope of the straight line. As shown in the inset of Figure 7b, the E_a of Cl-doped samples is obviously lower than Bi$_2$O$_2$Se, indicating that the introduction of Cl is conducive to carrier excitation. In summary, the high σ achieved in Cl-doped Bi$_2$O$_2$Se is estimated to be the result of higher n coupled with lower E_a.
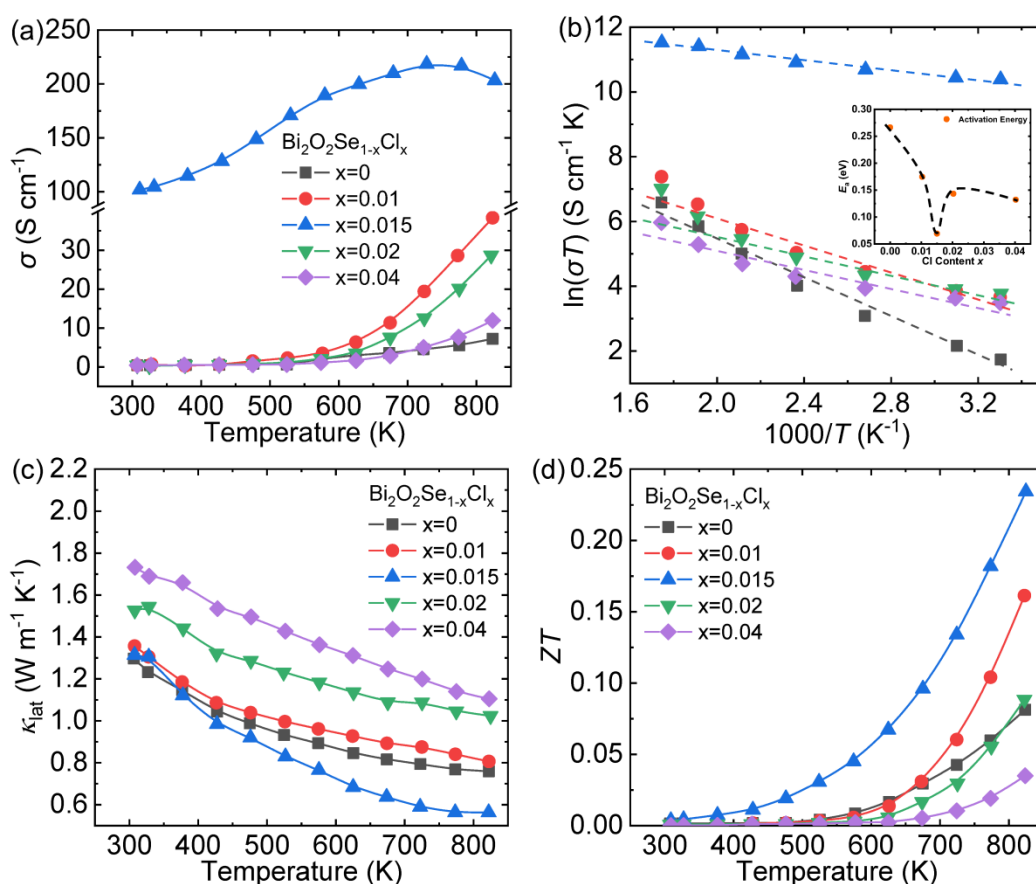
Figure 7. Thermoelectric transport properties of Bi$_2$O$_2$Se$_{1-x}$Cl$_x$ (x = 0–0.04): (**a**) electrical conductivity, (**b**) the fitting plots of the small polaron model and the activation energy (E_a) shown in the inset, (**c**) lattice thermal conductivity and (**d**) *ZT*. Data shown in (**a**–**d**) were adopted from Reference [51]. Copyright 2017, The American Ceramic Society.

Lattice thermal conductivity (κ_{lat}) of Bi$_2$O$_2$Se$_{0.985}$Cl$_{0.015}$ declines evidently after 423 K, reaching the lowest value ~0.56 W m^{-1} K^{-1} at 823 K (Figure 7c). This effective decrease in κ_{lat} is derived from point defect scattering introduced by Cl substitution coupled

with the enhanced grain boundaries scattering. However, for the $Bi_2O_2Se_{0.98}Cl_{0.02}$ and $Bi_2O_2Se_{0.96}Cl_{0.04}$ sample, the considerable augment in κ_{lat} is the result of the secondary phase $Bi_{12}O_{15}Cl_6$.

Benefitting from both the enhancement of the σ and the depression of the κ_{tot}, the peak ZT value ~0.23 at 823 K is achieved in $Bi_2O_2Se_{0.985}Cl_{0.015}$ (Figure 7d), which demonstrates that Cl is an effective dopant to optimize the thermoelectric performance of Bi_2O_2Se.

3.3. Doping Te at Se Sites

The ZT value of pristine Bi_2O_2Se is primarily restricted by the low electric conductivity (~2.0 S cm^{-1}) mainly caused by the low carrier concentration (~10^{15} cm^{-3}) [50,51]. Fundamentally, this shortcoming can be attributed to the excessively wide band gap (~1.28 eV) [71]. Bi_2O_2Te, an isostructure of Bi_2O_2Se, possesses a narrow band gap (~0.23 eV) and a moderately high room-temperature carrier concentration (~1.06×10^{18} cm^{-3}) [45]. Additionally, *p*-type BiCuTeO has a narrower band gap (~0.4 eV) compared with BiCuSeO (~0.8 eV) [72,73], and relevant studies have proved that Te substitution can effectively enhance the electrical conductivity of *p*-type BiCuSeO by narrowing the band gap [74]. Hence, isovalent Te doping at Se sites could be utilized to the *n*-type Bi_2O_2Se.

The significantly narrowed band gap is conducive for electrons to jump across the band gap and enter the valence band (Figure 8a) so that more electrons can be excited and participate in the electrical transport. The measured optical absorption spectrum of $Bi_2O_2Se_{1-x}Te_x$ ($x = 0.02, 0.03, 0.04, 0.06$) samples indicates that the band gap is monotonically reduced from ~1.77 eV for Bi_2O_2Se to ~0.78 eV for $Bi_2O_2Se_{0.94}Te_{0.06}$ with the increasing Te content (Figure 8b) [44]. Considering the apparent difference of the band gap between Bi_2O_2Se (~1.77 eV) and Bi_2O_2Te (~0.23 eV), the band gap engineering can be effectively tuned by a small amount of Te substitution.

Ultimately, the low carrier concentration of pristine Bi_2O_2Se (~10^{15} cm^{-3}) was boosted to ~10^{18} cm^{-3}, which was increased by three orders of magnitude [44]. The greatly increased carrier concentration makes the σ of all the Te-doped samples significantly larger than pristine Bi_2O_2Se throughout the entire test temperature range (Figure 8c).

To obtain insight into the electrical transport behavior, the small polaron hopping conduction theory mentioned in the previous work [70] was selected to analyze the electric conductivity. The strong linear correlation between $\ln(\sigma T)$ and $1000/T$ is exhibited in Figure 8d, and the curve of calculated activation energy E_a varying with the Te content is depicted in Figure 8e. The E_a of electronic conduction declines with the increasing Te content, indicating that the Te substitution is beneficial for the intrinsic excitation of electrons, thereby contributing to the optimized σ. Figure 8f plots the temperature dependence of ZT. Due to the increment in σ caused by the narrowing band gap, the thermoelectric performance of Bi_2O_2Se was enhanced. Ultimately, the highest ZT reaches ~0.28 at 823 K for $Bi_2O_2Se_{0.96}Te_{0.04}$.

3.4. Doping Ta at Bi Sites

Choosing a suitable dopant to enhance its low carrier concentration has always been an important means to optimize the thermoelectric performance of the Bi_2O_2Se system. A pentavalent Ta^{5+} cation doping at Bi sites will provide two extra electrons for the matrix. Moreover, Ta is less electronegative than Bi, thereby easily extracting electrons. Therefore, Tan et al. chose Ta as the dopant to increase the carrier concentration, thereby enhancing the electrical transport properties of Bi_2O_2Se [68].

Ta doping can significantly increase the σ of Bi_2O_2Se, from ~0.02 S cm^{-1} of pristine Bi_2O_2Se to ~149.3 S cm^{-1} of $Bi_{1.90}Ta_{0.10}O_2Se$ at room temperature (Figure 9a). Meanwhile, the temperature-dependent σ transform from semiconductor behavior to mixed-conducting behavior, and finally, $Bi_{1.90}Ta_{0.10}O_2Se$ and $Bi_{1.88}Ta_{0.12}O_2Se$ even exhibit degenerate semiconductor behavior. The carrier concentration (n_H) and mobility (μ_H) were measured and exhibited in Figure 9b. Ta doping increases the n_H by four orders of magnitude, from ~10^{15} cm^{-3} to ~10^{19} cm^{-3}. In addition to the reason that Ta replaces Bi to provide extra

electrons, authors believe that the formation of the Ta_2O_5 phase will introduce oxygen vacancies into the matrix, and each oxygen vacancy is compensated by two electrons as the following formula:

$$V_O^\times \rightarrow V_O^{\cdot\cdot} + 2e'$$
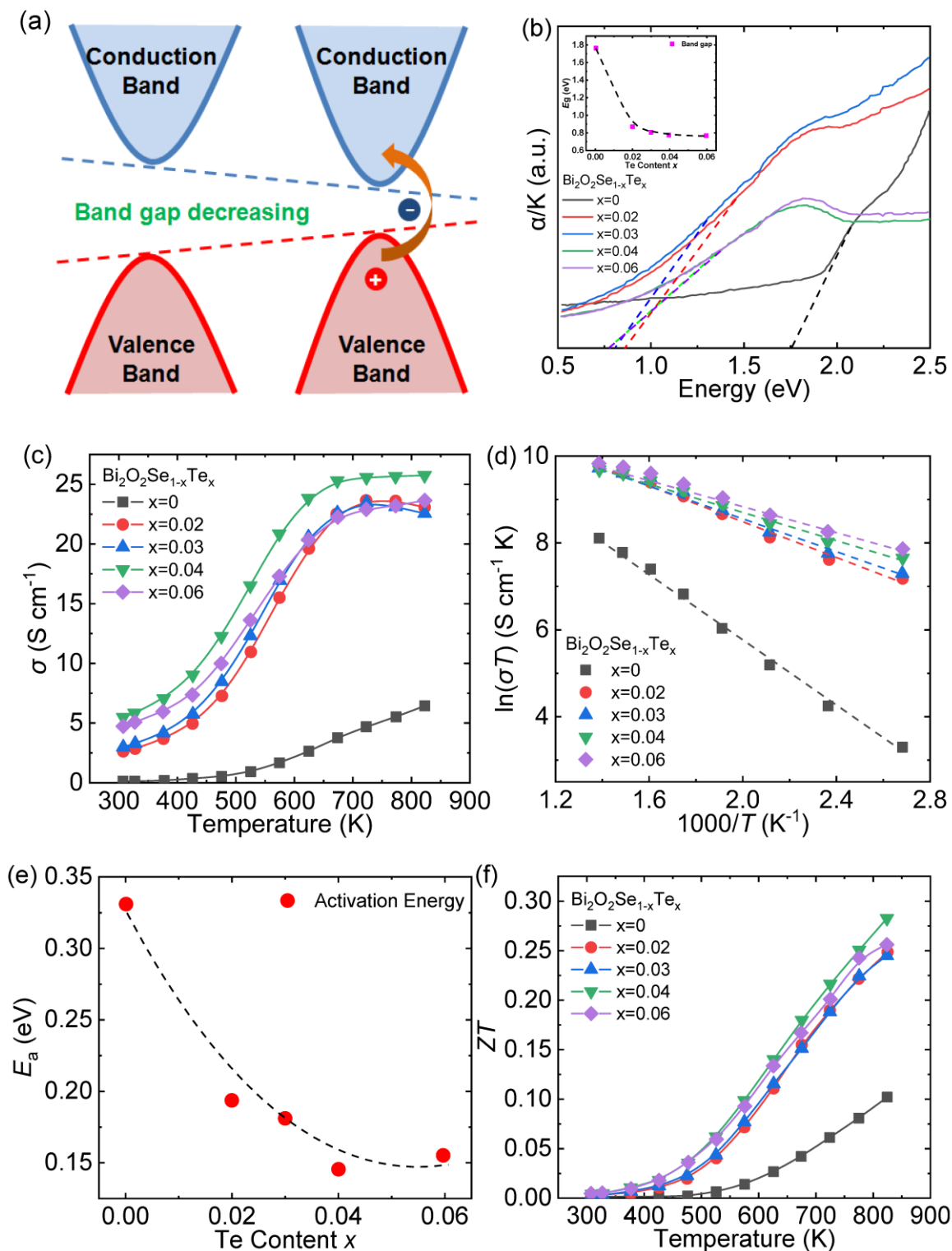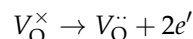
Figure 8. (**a**) The schematic diagram of narrowing the band gap; (**b**) the optical absorption spectra of $Bi_2O_2Se_{1-x}Te_x$ (*x* = 0–0.06) and the band gap varying with Te content shown in the inset; (**c**) electrical conductivity, (**d**) the fitting plot of the electrical conductivity by the small polaron model, (**e**) the activation energy (E_a) and (**f**) *ZT* of $Bi_2O_2Se_{1-x}Te_x$ (*x* = 0–0.06). Data shown in (**b**–**f**) were adopted from Reference [44]. Copyright 2017, The American Ceramic Society.
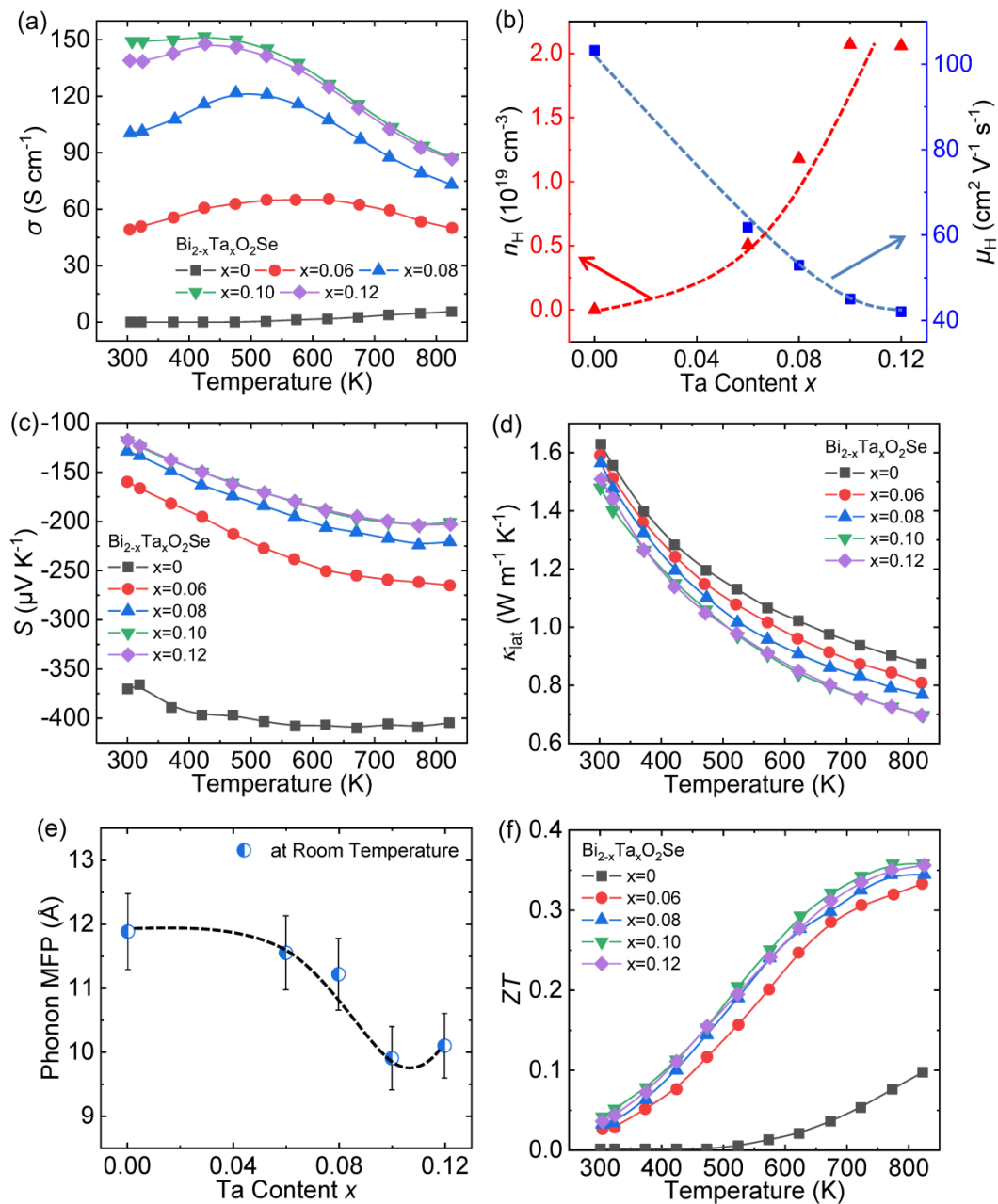
Figure 9. Thermoelectric transport properties of $Bi_{2-x}Ta_xO_2Se$ (x = 0–0.12): (**a**) electrical conductivity, (**b**) the carrier concentration and mobility at room temperature, (**c**) Seebeck coefficient, (**d**) lattice thermal conductivity, (**e**) phonon mean free path (MPF, l_{ph}) at room temperature, and (**f**) ZT. Data shown in (**a**–**f**) were adopted from Reference [68]. Copyright 2019, WILEY-VCH Verlag GmbH & Co. KGaA, Weinheim.

Therefore, both Ta doping and oxygen vacancies lead to the increment of n_H. Simultaneously, the stable deterioration of μ_H implies gradually reinforced carrier scattering, but relatively high μ_H (>40 cm^2 V^{-1} s^{-1}) can be maintained, which is because performing Ta at Bi sites would not introduce lattice defects into the conductive [Se]$^{2-}$ layers.

Compared with pristine Bi_2O_2Se, the absolute value of S decreases when the Ta content increases (Figure 9c), which is coincident with the increase in n_H. The calculated weighted mobility ($\mu m^{*3/2}$) is greatly increased from ~5.41 $m_0^{3/2}$ cm^2 V^{-1} s^{-1} for Bi_2O_2Se to ~15.44 $m_0^{3/2}$ cm^2 V^{-1} s^{-1} for $Bi_{1.90}Ta_{0.10}O_2Se$, revealing that Ta doping in Bi_2O_2Se can effectively optimize the electrical transport properties.

The κ_{lat} continuously decreases as the Ta content increases, reaching ~0.69 W m^{-1} K^{-1} for Bi$_{1.88}$Ta$_{0.12}$O$_2$Se at 823 K (Figure 9d). The phonon mean-free-path (l_{ph}) is calculated by the following Formula (6) [75,76] and plotted in Figure 9e as a function of Ta content.

$$\kappa_{lat} = \frac{1}{3} C_v v_a l_{ph} \tag{6}$$

where, C_v and v_a represent the specific heat capacity per unit volume and average sound speed, respectively. A highly intense phonon scattering process and decrease of κ_{lat} in Ta-doped Bi$_2$O$_2$Se can be seen from monotonically reduced l_{ph} from ~11.9 Å for Bi$_2$O$_2$Se to ~9.9 Å for Bi$_{1.90}$Ta$_{0.10}$O$_2$Se, which mainly results from that Ta substitution introduces multi-scale lattice defects, including the enormous defects, grain boundaries, and phase interfaces [68,77].

The carrier engineering and hierarchical microstructure by Ta doping remarkably enhance the *ZT* values in Bi$_{1.90}$Ta$_{0.10}$O$_2$Se, reaching ~0.30 at 773 K, which is an increase of ~350% compared to pristine Bi$_2$O$_2$Se (Figure 9f).

4. Attempts to Realize a New Kind of *n*-Type Oxyselenide: Bi$_6$Cu$_2$Se$_4$O$_6$

Because of the strong phonon scattering caused by layered structure [9], the lone pair electrons of Bi^{3+} [78,79], and the local vibration of Cu$^+$ [38], BiCuSeO exhibits inherent low thermal conductivity. Another well-known thermoelectric oxyselenide, Bi$_2$O$_2$Se reveals stable *n*-type transport properties due to Se vacancies [43,44]. To fully utilize the features of BiCuSeO and Bi$_2$O$_2$Se, a new type layered oxyselenide Bi$_6$Cu$_2$Se$_4$O$_6$ was synthesized through solid state reaction (SSR) with the 1:2 ratio of BiCuSeO and Bi$_2$O$_2$Se (Figure 10a) [28–30], and stable *n*-type conductive transports were observed in this system through halogen element doping [29].

4.1. Halogen Element Doping at Se Sites

The σ of Cl-doped Bi$_6$Cu$_2$Se$_4$O$_6$ is higher than Br-doped one at high temperature for the doping content $x = 0.2$. When the doping content x is increased to 0.8, the σ was significantly improved to ~70 S cm^{-1}, and the Br-doped sample was better σ than the Cl-doped one at high temperature (Figure 10b). The Bi$_6$Cu$_2$Se$_{3.8}$Br$_{0.2}$O$_6$ exhibits *p*-type semiconductor characteristics below 673 K and transfer to *n*-type with the temperature increasing; while Bi$_6$Cu$_2$Se$_{3.8}$Cl$_{0.2}$O$_6$ has a negative *S* value within the entire temperature boundaries indicating that a small amount of Cl doping ($x = 0.2$) can achieve stable *n*-type semiconductor behavior (Figure 10c). When the doing content raises up to 0.8, the *S* of Cl/Br-doped samples has little difference, varying from ~−60 to −160 µV K^{-1}. The maximum *ZT* value ~0.15 at 823 K is achieved in Bi$_6$Cu$_2$Se$_{3.2}$Br$_{0.8}$O$_6$ (Figure 10c).

4.2. Transition Metal Element Doping at Bi Sites

Zheng et al. chose Bi$_6$Cu$_2$Se$_{3.6}$Cl$_{0.4}$O$_6$ as the matrix and doped transition metal elements (Zr, Ti and Ce) at Bi sites to enhance its thermoelectric performance [30]. The introduction of transition metal elements can effectively increase the carrier concentration (n_H) and maintain the carrier mobility (μ_H; Figure 11a), thereby optimizing the electric conductivity (σ) of the matrix. The *S* of all doped samples remains negative throughout the entire temperature range, indicating the stable *n*-type semiconductor properties (Figure 11b). Thanks to the optimized σ and maintained *S*, the power factor (*PF*) is effectively enhanced (Figure 11c). Finally, due to the enhanced electrical transport properties and reduced thermal conductivity [30], the peak *ZT* value reached ~0.16 at 873 K in Bi$_{5.9}$Zr$_{0.1}$Cu$_2$Se$_{3.6}$Cl$_{0.4}$O$_6$ (Figure 11d), which is 60% higher than that in Bi$_6$Cu$_2$Se$_{3.6}$Cl$_{0.4}$O$_6$ (~0.10 at 873 K).

As a new type of layered oxyselenide thermoelectric material, Bi$_6$Cu$_2$Se$_4$O$_6$ maintains the advantages of BiCuSeO and Bi$_2$O$_2$Se, such as lower-cost and nontoxic elements, better thermal and chemical stability. Moreover, Bi$_6$Cu$_2$Se$_4$O$_6$ can exhibit stable *n*-type semiconductor behavior by simple halogen doping and has intrinsic low thermal conductivity

due to complex crystal structure. Thereby, $Bi_6Cu_2Se_4O_6$ is a new kind of *n*-type layered oxyselenide thermoelectric material with broad development prospects.
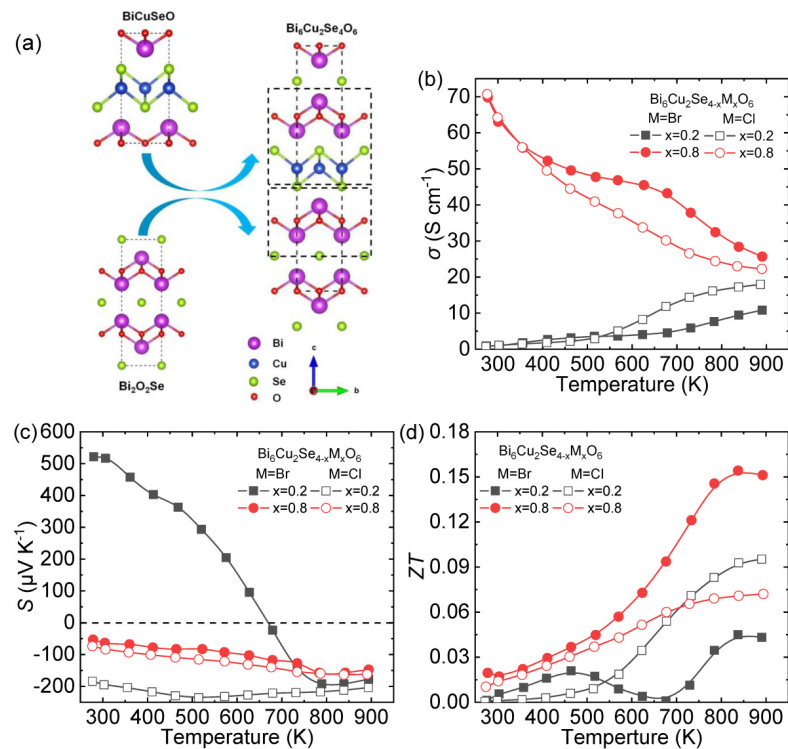
Figure 10. (**a**) The crystal structure of $Bi_6Cu_2Se_4O_6$. The temperature dependence of thermoelectric transport properties for $Bi_6Cu_2Se_{4-x}M_xO_6$ (M = Cl/Br, *x* = 0.2/0.8): (**b**) electrical conductivity, (**c**) Seebeck coefficient, (**d**) *ZT*. Data shown in (**b**–**d**) were adopted from Reference [29]. Copyright 2019, WILEY-VCH Verlag GmbH & Co. KGaA, Weinheim.
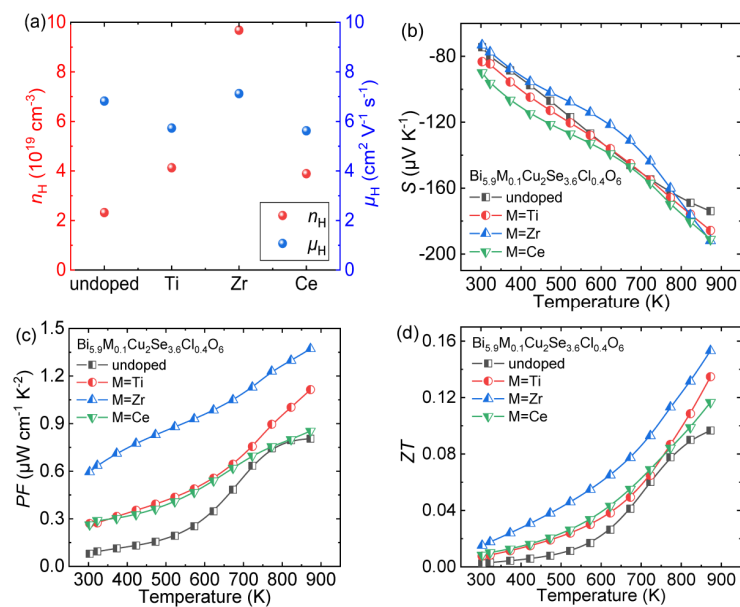
Figure 11. Thermoelectric transport properties of $Bi_6Cu_2Se_{3.6}Cl_{0.4}O_6$ and $Bi_{5.9}M_{0.1}Cu_2Se_{3.6}Cl_{0.4}O_6$ (M = Ti, Zr, Ce): (**a**) carrier concentration (n_H) and mobility (μ_H) at room temperature, (**b**) Seebeck coefficient, (**c**) power factor and (**d**) *ZT*. Data shown in (**b**–**d**) were adopted from Reference [30]. Copyright 2021, Acta Materialia Inc.

5. Summary and Perspective

In this short review, we introduced the latest accomplishments in *n*-type layered oxyselenide thermoelectric materials, including BiCuSeO, Bi_2O_2Se and $Bi_6Cu_2Se_4O_6$. For BiCuSeO, many strategies have been used to enhance the thermoelectric performance of *p*-type systems, but there are few studies on *n*-type BiCuSeO, and it is difficult to obtain stable *n*-type semiconductor behavior. For Bi_2O_2Se, carrier engineering, band engineering, microstructure design, etc., achieved performance enhancements of Bi_2O_2Se, but the *ZT* value is still limited to 0.4 [68]. Moreover, a new kind of promising *n*-type transport properties can be obtained in layered oxyselenide $Bi_6Cu_2Se_4O_6$ through halogen element doping. Apart from the advancements mentioned above, there is still room left for further research, such as make full utilization of the anisotropic transport properties of those compounds through texturing microstructure and crystals growth.

Author Contributions: All the authors co-edited and wrote the paper. All authors have read and agreed to the published version of the manuscript.

Institutional Review Board Statement: Not applicable.

Informed Consent Statement: Not applicable.

Data Availability Statement: The data of this study are available from the corresponding author upon reasonable request.

Conflicts of Interest: The authors declare no conflict of interest.

References

1. Zhang, X.; Zhao, L.-D. Thermoelectric materials: Energy conversion between heat and electricity. *J. Mater.* **2015**, *1*, 92–105. [CrossRef]
2. Zhao, L.-D.; He, J.; Berardan, D.; Lin, Y.; Li, J.-F.; Nan, C.-W.; Dragoe, N. BiCuSeO oxyselenides: New promising thermoelectric materials. *Energy Environ. Sci.* **2014**, *7*, 2900–2924. [CrossRef]
3. Li, J.F.; Liu, W.S.; Zhao, L.-D.; Min, Z. High-performance nanostructured thermoelectric materials. *NPG Asia Mater.* **2010**, *2*, 152–158. [CrossRef]
4. Snyder, G.J.; Toberer, E.S. Complex thermoelectric materials. *Nat. Mater.* **2008**, *7*, 105–114. [CrossRef]
5. Di, W.; Pei, Y.; Zhe, W.; Wu, H.; Li, H.; Zhao, L.-D.; He, J. Significantly enhanced thermoelectric performance in *n*-type heterogeneous BiAgSeS composites. *Adv. Funct. Mater.* **2015**, *24*, 7763–7771.
6. Qin, B.C.; Wang, D.Y.; He, W.K.; Zhang, Y.; Wu, H.; Pennycook, S.J.; Zhao, L.D. Realizing high thermoelectric performance in *p*-type SnSe through crystal structure modification. *J. Am. Chem. Soc.* **2018**, *141*, 1141–1149. [CrossRef] [PubMed]
7. Kim, S.I.; Lee, K.H.; Mun, H.A.; Kim, H.S.; Hwang, S.W.; Roh, J.W.; Yang, D.J.; Shin, W.H.; Li, X.S.; Lee, Y.H. Dense dislocation arrays embedded in grain boundaries for high-performance bulk thermoelectrics. *Science* **2015**, *348*, 109–114. [CrossRef]
8. Chung, D.Y.; Hogan, T.; Brazis, P.; Rocci-Lane, M.; Kannewurf, C.; Bastea, M.; Uher, C.; Kanatzidis, M.G. $CsBi_4Te_6$: A high-performance thermoelectric material for low-temperature applications. *Science* **2000**, *287*, 1024–1027. [CrossRef]
9. Venkatasubramanian, R.; Silvola, E.; Colpitts, T.; O'Quinn, B. Thin-film thermoelectric devices with high room-temperature figures of merit. *Nature* **2001**, *413*, 597–602. [CrossRef]
10. Biswas, K.; Zhao, L.-D.; Kanatzidis, M.G. Tellurium-free thermoelectric: The anisotropic *n*-type semiconductor Bi_2S_3. *Adv. Energy Mater.* **2012**, *2*, 634–638. [CrossRef]
11. Tan, G.; Shi, F.; Hao, S.; Zhao, L.-D.; Kanatzidis, M.G. Non-equilibrium processing leads to record high thermoelectric figure of merit in PbTe–SrTe. *Nat. Commun.* **2016**, *7*, 12167. [CrossRef]
12. Heremans, J.P.; Jovovic, V.; Toberer, E.S.; Saramat, A.; Kurosaki, K.; Charoenphakdee, A.; Yamanaka, S.; Snyder, G.J. Enhancement of thermoelectric efficiency in PbTe by distortion of the electronic density of states. *Science* **2008**, *321*, 554–557. [CrossRef]
13. Qin, B.C.; Xiao, Y.; Zhou, Y.M.; Zhao, L.-D. Thermoelectric transport properties of Pb-Sn-Te-Se system. *Rare Metals* **2018**, *37*, 343–350. [CrossRef]

14. Xiao, Y.; Wu, H.; Cui, J.; Wang, D.; Fu, L.; Zhang, Y.; Chen, Y.; He, J.; Pennycook, S.J.; Zhao, L.-D. Realizing high performance *n*-type PbTe by synergistically optimizing effective mass and carrier mobility and suppressing bipolar thermal conductivity. *Energy Environ. Sci.* **2018**, *11*, 2486–2495. [CrossRef]

15. Xiao, Y.; Zhao, L.-D. Charge and phonon transport in PbTe-based thermoelectric materials. *NPJ Quantum Mater.* **2018**, *3*, 55. [CrossRef]

16. Zhang, X.; Wang, D.; Wu, H.; Yin, M.; Pei, Y.; Gong, S.; Huang, L.; Pennycook, S.J.; He, J.; Zhao, L.-D. Simultaneously enhancing the power factor and reducing the thermal conductivity of SnTe via introducing its analogues. *Energy Environ. Sci.* **2017**, *10*, 2420–2431. [CrossRef]

17. Zhao, H.; Sui, J.; Tang, Z.; Lan, Y.; Ren, Z. High thermoelectric performanceof MgAgSb-based materials. *Nano Energy* **2014**, *7*, 97–103. [CrossRef]

18. Li, D.; Zhao, H.; Li, S.; Wei, B.; Shuai, J.; Shi, C.; Xi, X.; Sun, P.; Meng, S.; Gu, L. Atomic disorders induced by silver and magnesium ion migrations favor high thermoelectric performance in *α*-MgAgSb-based materials. *Adv. Funct. Mater.* **2015**, *25*, 6478–6488. [CrossRef]

19. Liu, Z.; Wang, Y.; Mao, J.; Geng, H.; Shuai, J.; Wang, Y.; He, R.; Cai, W.; Sui, J.; Ren, Z. Lithium doping to enhance thermoelectric performance of MgAgSb with weak electron–phonon coupling. *Adv. Energy Mater.* **2016**, *6*, 1502269. [CrossRef]

20. Makongo, J.P.A.; Misra, D.K.; Zhou, X.; Pant, A.; Shabetai, M.R.; Su, X.; Uher, C.; Stokes, K.L.; Poudeu, P.F.P. Simultaneous large enhancements in thermopower and electrical conductivity of bulk nanostructured half-Heusler alloys. *J. Am. Chem. Soc.* **2011**, *133*, 18843–18852. [CrossRef]

21. Chen, S.; Ren, Z. Recent progress of half-Heusler for moderate temperature thermoelectric applications. *Mater. Today* **2013**, *16*, 387–395. [CrossRef]

22. Xie, H.; Wang, H.; Pei, Y.; Fu, C.; Zhu, T. Beneficial contribution of alloy disorder to electron and phonon transport in half-Heusler thermoelectric materials. *Adv. Funct. Mater.* **2013**, *23*, 5123–5130. [CrossRef]

23. Young, D.M.; Torardi, C.C.; Olmstead, M.M.; Kauzlarich, S.M. Exploring the limits of the Zintl concept for the $A_{14}MPn_{11}$ structure type with M = Zn, Cd. *Chem. Mater.* **1995**, *7*, 93–101. [CrossRef]

24. Toberer, E.S.; May, A.F.; Scanlon, C.J.; Snyder, G.J. Thermoelectric properties of *p*-type LiZnSb: Assessment of ab initio calculations. *J. Appl. Phys.* **2009**, *105*, 063706. [CrossRef]

25. Zhang, X.X.; Chang, C.; Zhou, Y.M.; Zhao, L.-D. BiCuSeO thermoelectrics: An update on recent progress and perspective. *Materials* **2017**, *10*, 198. [CrossRef]

26. Ruleova, P.; Drasar, C.; Lostak, P.; Li, C.P.; Ballikaya, S.; Uher, C. Thermoelectric properties of Bi_2O_2Se. *Mater. Chem. Phys.* **2010**, *119*, 299–302. [CrossRef]

27. Zhang, K.; Hu, C.; Kang, X.; Wang, S.; Yi, X.; Hong, L. Synthesis and thermoelectric properties of Bi_2O_2Se nanosheets. *Mater. Res. Bull.* **2013**, *48*, 3968–3972. [CrossRef]

28. Gibson, Q.D.; Dyer, M.S.; Robertson, C.; Delacotte, C.; Manning, T.D.; Pitcher, M.J.; Daniels, L.M.; Zanella, M.; Alaria, J.; Claridge, J.B.; et al. $Bi_{2+2n}O_{2+2n}Cu_{2-\delta}Se_{2+n-\delta}X_\delta$ (X = Cl, Br): A three-anion homologous series. *Inorg. Chem.* **2018**, *57*, 12489–12500. [CrossRef]

29. Zhang, X.X.; Qiu, Y.T.; Ren, D.D.; Zhao, L.-D. Electrical and thermal transport properties of *n*-type $Bi_6Cu_2Se_4O_6$ ($2BiCuSeO + 2Bi_2O_2Se$). *Ann. Phys.* **2019**, *532*, 1900340. [CrossRef]

30. Zheng, J.Q.; Wang, D.Y.; Zhao, L.-D. Enhancing thermoelectric performance of *n*-type $Bi_6Cu_2Se_4O_6$ through introducing transition metal elements. *Scr. Mater.* **2021**, *202*, 114010. [CrossRef]

31. Koumoto, K.; Funahashi, R.; Guilmeau, E.; Miyazaki, Y.; Weidenkaff, A.; Wang, Y.F.; Wan, C.L. Thermoelectric ceramics for energy harvesting. *J. Am. Ceram. Soc.* **2013**, *96*, 1–23. [CrossRef]

32. Berdonosov, P.S.; Kusainova, A.M.; Kholodkovskaya, L.N.; Dolgikh, V.A.; Akselrud, L.G.; Popovkin, B.A. Powder X-ray and IR studies of the new oxyselenides MOCuSe (M = Bi, Gd, Dy). *J. Solid State Chem.* **1995**, *118*, 74–77. [CrossRef]

33. Hiramatsu, H.; Kamioka, H.; Ueda, K.; Hirano, M.; Hosono, H. Electrical and photonic functions originating from low-dimensional structures in wide-gap semiconductors LnCuOCh (Ln=lanthanide, Ch=chalcogen): A review. *J. Ceram. Soc. Jpn.* **2005**, *113*, 10–16. [CrossRef]

34. Kamioka, H.; Hiramatsu, H.; Hirano, M.; Ueda, K.; Kamiya, T.; Hosono, H. Excitonic properties related to valence band levels split by spin–orbit interaction in layered oxychalcogenide LaCuOCh(Ch=S,Se). *J. Lumin.* **2005**, *112*, 66–70. [CrossRef]

35. Clarke, D.R. Materials selection guidelines for low thermal conductivity thermal barrier coatings. *Surf. Coat. Technol.* **2003**, *163*, 67–74. [CrossRef]

36. Qu, W.W.; Zhang, X.X.; Yuan, B.F.; Zhao, L.-D. Homologous layered $InFeO_3(ZnO)_m$: New promising abradable seal coating materials. *Rare Metals* **2018**, *37*, 79–94. [CrossRef]

37. Zhou, Y.M.; Zhao, L.-D. Promising thermoelectric bulk materials with 2D structures. *Adv. Mater.* **2017**, *29*, 14. [CrossRef] [PubMed]

38. Vaqueiro, P.; Al Orabi, R.A.; Luu, S.D.; Guelou, G.; Powell, A.V.; Smith, R.I.; Song, J.P.; Wee, D.; Fornari, M. The role of copper in the thermal conductivity of thermoelectric oxychalcogenides: Do lone pairs matter? *Phys. Chem. Chem. Phys.* **2015**, *17*, 31735–31740. [CrossRef] [PubMed]

39. Saha, S.K. Exploring the origin of ultralow thermal conductivity in layered BiOCuSe. *Phys. Rev. B* **2015**, *92*, 041202. [CrossRef]

40. Kanatzidis, M.G. Nanostructured thermoelectrics: The new paradigm? *Chem. Mater.* **2010**, *22*, 648–659. [CrossRef]

41. Pei, Y.L.; Chang, C.; Wang, Z.; Yin, M.J.; Wu, M.H.; Tan, G.J.; Wu, H.J.; Chen, Y.X.; Zheng, L.; Gong, S.; et al. Multiple converged conduction bands in $K_2Bi_8Se_{13}$: A promising thermoelectric material with extremely low thermal conductivity. *J. Am. Chem. Soc.* **2016**, *138*, 16364–16371. [CrossRef] [PubMed]

42. Chang, C.; Zhao, L.-D. Anharmoncity and low thermal conductivity in thermoelectrics. *Mater. Today Phys.* **2018**, *4*, 50–57. [CrossRef]

43. Pan, L.; Zhao, L.; Zhang, X.; Chen, C.; Wang, Y. Significant optimization of electron-phonon transport of *n*-Type Bi_2O_2Se by mechanical manipulation of Se vacancies *via* shear exfoliation. *ACS Appl. Mater. Interfaces* **2019**, *11*, 21603–21609. [CrossRef]

44. Tan, X.; Li, Y.C.; Hu, K.R.; Ren, G.K.; Li, Y.M. Synergistically optimizing electrical and thermal transport properties of Bi_2O_2Se ceramics by Te-substitution. *J. Am. Ceram. Soc.* **2017**, *101*, 326–333. [CrossRef]

45. Luu, S.; Vaqueiro, P. Synthesis, characterisation and thermoelectric properties of the oxytelluride Bi_2O_2Te. *J. Solid State Chem.* **2015**, *226*, 219–223. [CrossRef]

46. Zhan, B.; Liu, Y.; Xing, T.; Lan, J.L.; Lin, Y.H.; Nan, C.W. Enhanced thermoelectric properties of Bi_2O_2Se ceramics by Bi deficiencies. *J. Am. Ceram. Soc.* **2015**, *98*, 2465–2469. [CrossRef]

47. Zhan, B.; Butt, S.; Liu, Y.C.; Lan, J.L.; Nan, C.W.; Lin, Y.H. High-temperature thermoelectric behaviors of Sn-doped *n*-type Bi_2O_2Se ceramics. *J. Electroceram.* **2015**, *34*, 175–179. [CrossRef]

48. Zhan, B.; Liu, Y.; Lan, J.; Zeng, C.; Lin, Y.H.; Nan, C.W. Enhanced thermoelectric performance of Bi_2O_2Se with Ag addition. *Materials* **2015**, *8*, 1568–1576. [CrossRef]

49. Wang, D.Y.; Huang, Z.W.; Zhang, Y.; Hao, L.J.; Zhao, L.-D. Extremely low thermal conductivity from bismuth selenohalides with 1D soft crystal structure. *Sci. China Mater.* **2020**, *83*, 1759–1768. [CrossRef]

50. Liu, R.; Lan, J.L.; Tan, X.; Liu, Y.C.; Ren, G.K.; Liu, C.; Zhou, Z.F.; Nan, C.W.; Lin, Y.H. Carrier concentration optimization for thermoelectric performance enhancement in *n*-type Bi_2O_2Se. *J. Eur. Ceram. Soc.* **2018**, *38*, 2742–2746. [CrossRef]

51. Tan, X.; Lan, J.L.; Ren, G.; Liu, Y.; Nan, C.W. Enhanced thermoelectric performance of *n*-type Bi_2O_2Se by Cl-doping at Se site. *J. Am. Ceram. Soc.* **2017**, *98*, 1494–1501. [CrossRef]

52. Pan, L.; Lang, Y.D.; Zhao, L.; Berardan, D.; Amzallag, E.; Xu, C.; Gu, Y.F.; Chen, C.C.; Zhao, L.-D.; Shen, X.D.; et al. Realization of *n*-type and enhanced thermoelectric performance of *p*-type BiCuSeO by controlled iron incorporation. *J. Mater. Chem. A* **2018**, *6*, 13340–13349. [CrossRef]

53. Goldsmid, H.J.; Sharp, J.W. Estimation of the thermal band gap of a semiconductor from Seebeck measurements. *J. Electron. Mater.* **1999**, *28*, 869–872. [CrossRef]

54. Gibbs, Z.M.; Kim, H.S.; Wang, H.; Snyder, G.J. Band gap estimation from temperature dependent Seebeck measurement—deviations from the $2e|S|_{max}T_{max}$ relation. *Appl. Phys. Lett.* **2015**, *106*, 869–872. [CrossRef]

55. Tan, S.G.; Gao, C.H.; Wang, C.; Sun, Y.P.; Jing, Q.; Meng, Q.K.; Zhou, T.; Ren, J.F. Realization of *n*-type BiCuSeO through Co doping. *Solid State Sci.* **2019**, *98*, 106019. [CrossRef]

56. Bardeen, J.; Shockley, W.S. Deformation potentials and mobilities in non-polar crystals. *Phys. Rev.* **1950**, *80*, 72–80. [CrossRef]

57. Goldsmid, H.J. *Introduction to Thermoelectricity*; Springer: Berlin, Germany, 2009; pp. 339–357.

58. Pei, Y.L.; He, J.; Li, J.F.; Li, F.; Liu, Q.; Pan, W.; Barreteau, C.; Berardan, D.; Dragoe, N.; Zhao, L.-D. High thermoelectric performance of oxyselenides: Intrinsically low thermal conductivity of Ca-doped BiCuSeO. *NPG Asia Mater.* **2013**, *5*, e47. [CrossRef]

59. Barreteau, C.; Bérardan, D.; Amzallag, E.; Zhao, L.-D.; Dragoe, N. Structural and electronic transport properties in Sr-doped BiCuSeO. *Chem. Mater.* **2012**, *24*, 3168–3178. [CrossRef]

60. Yang, J.M.; Yang, G.; Zhang, G.B.; Wang, Y.X. Low effective mass leading to an improved ZT value by 32% for *n*-type BiCuSeO: A first-principles study. *J. Mater. Chem. A* **2014**, *2*, 13923–13931. [CrossRef]

61. Zhang, X.X.; Feng, D.; He, J.Q.; Zhao, L.-D. Attempting to realize *n*-type BiCuSeO. *J. Solid State Chem.* **2018**, *258*, 510–516. [CrossRef]

62. Li, Z.; Xiao, C.; Fan, S.J.; Deng, Y.; Zhang, W.S.; Ye, B.J.; Xie, Y. Dual vacancies: An effective strategy realizing synergistic optimization of thermoelectric property in BiCuSeO. *J. Am. Chem. Soc.* **2015**, *137*, 6587–6593. [CrossRef]

63. Liu, Y.; Zhao, L.-D.; Liu, Y.C.; Lan, J.L.; Xu, W.; Li, F.; Zhang, B.-P.; Berardan, D.; Dragoe, N.; Lin, Y.-H.; et al. Remarkable enhancement in thermoelectric performance of BiCuSeO by Cu deficiencies. *J. Am. Chem. Soc.* **2011**, *133*, 20112–20115. [CrossRef]

64. Yu, B.; Liu, W.S.; Chen, S.; Wang, H.; Wang, H.Z.; Chen, G.; Ren, Z.F. Thermoelectric properties of copper selenide with ordered selenium layer and disordered copper layer. *Nano Energy* **2012**, *1*, 472–478. [CrossRef]

65. Liu, H.; Shi, X.; Xu, F.; Zhang, L.; Zhang, W.; Chen, L.; Li, Q.; Uher, C.; Day, T.; Snyder, G.J. Copper ion liquid-like thermoelectrics. *Nat. Mater.* **2012**, *11*, 422–425. [CrossRef]

66. Zhang, X.X.; Wang, D.Y.; Wang, G.T.; Zhao, L.-D. Realizing *n*-type BiCuSeO through halogens doping. *Ceram. Int.* **2019**, *45*, 14953–14957. [CrossRef]

67. Tang, G.; Yang, C.; Stroppa, A.; Fang, D.; Hong, J. Revealing the role of thiocyanate anion in layered hybrid halide perovskite $(CH_3NH_3)_2Pb(SCN)_2I_2$. *J. Chem. Phys.* **2017**, *146*, 224702. [CrossRef] [PubMed]

68. Tan, X.; Liu, Y.C.; Liu, R.; Zhou, Z.F.; Liu, C.; Lan, J.L.; Zhang, Q.H.; Lin, Y.H.; Nan, C.W. Synergistical enhancement of thermoelectric properties in *n*-type Bi_2O_2Se by carrier engineering and hierarchical microstructure. *Adv. Energy Mater.* **2019**, *9*, 1900354. [CrossRef]

69. Myung, Y.; Wu, F.; Banerjee, S.; Stoica, A.; Zhong, H.X.; Lee, S.S.; Fortner, J.D.; Yang, L.; Banerjee, P. Highly conducting, *n*-type $Bi_{12}O_{15}Cl_6$ nanosheets with superlattice-like structure. *Cheminform* **2016**, *47*, 22–27. [CrossRef]

70. Bosman, A.; van Daal, H.J. Small-polaron versus band conduction in some transition-metal oxides. *Adv. Phys.* **1970**, *19*, 1–117. [CrossRef]

71. Guo, D.L.; Hu, C.G.; Xi, Y.; Zhang, K.Y. Strain effects to optimize thermoelectric properties of doped Bi_2O_2Se via tran–Blaha modified Becke–Johnson density functional theory. *J. Phys. Chem. C* **2013**, *117*, 21597–21602. [CrossRef]

72. Hiramatsu, H.; Yanagi, H.; Kamiya, T.; Ueda, K.; Hosono, H. Crystal structures, optoelectronic properties, and electronic structures of layered oxychalcogenides MCuOCh (M = Bi, La; Ch = S, Se, Te): Effects of electronic configurations of M^{3+} Ions. *Chem. Mater.* **2007**, *20*, 326–334. [CrossRef]

73. Vaqueiro, P.; Guélou, G.; Stec, M.; Guilmeau, E.; Powell, A.V. A copper-containing oxytelluride as a promising thermoelectric material for waste heat recovery. *J. Mater. Chem. A* **2013**, *1*, 520–523. [CrossRef]

74. Liu, Y.; Lan, J.L.; Xu, W.; Liu, Y.C.; Pei, Y.L.; Cheng, B.; Liu, D.B.; Lin, Y.H.; Zhao, L.-D. Enhanced thermoelectric performance of a BiCuSeO system via band gap tuning. *Chem. Commun.* **2013**, *49*, 8075–8077. [CrossRef]

75. Kurosaki, K.; Kosuga, A.; Muta, H.; Uno, M.; Yamanaka, S. Ag_9TlTe_5: A high-performance thermoelectric bulk material with extremely low thermal conductivity. *Appl. Phys. Lett.* **2005**, *87*, 061919. [CrossRef]

76. Tritt, T.M.; Subramanian, M.A.; Editors, G.J.M.B. Thermoelectric materials, phenomena, and applications: A bird's eye view. *MRS Bull.* **2006**, *31*, 188–198. [CrossRef]

77. Qin, B.C.; Wang, D.Y.; Zhao, L.-D. Slowing down the heat in thermoelectrics. *InfoMat* **2021**, *3*, 755–789. [CrossRef]

78. Zhao, L.-D.; Lo, S.H.; Zhang, Y.; Sun, H.; Tan, G.; Uher, C.; Wolverton, C.; Dravid, V.P.; Kanatzidis, M.G. Ultralow thermal conductivity and high thermoelectric figure of merit in SnSe crystals. *Nature* **2014**, *508*, 373–377. [CrossRef] [PubMed]

79. Skoug, E.J.; Cain, J.D.; Morelli, D.T. High thermoelectric figure of merit in the Cu_3SbSe_4-Cu_3SbS_4 solid solution. *Appl. Phys. Lett.* **2011**, *98*, 6029. [CrossRef]